

# Training Neural Networks with Optimal Double-Bayesian Learning

Vy Bui\*, Hang Yu\*, Karthik Kantipudi†, Ziv Yaniv† and Stefan Jaeger\*

\* Lister Hill National Center for Biomedical Communications, National Library of Medicine

National Institutes of Health, Bethesda, MD 20894, USA

†Office of Cyber Infrastructure and Computational Biology, National Institute of Allergy and Infectious Diseases

National Institutes of Health, Bethesda, MD 20892, USA

**Index Terms**—Machine learning, hyperparameter optimization, Bayes theorem, information theory, gradient descent, learning rate, momentum, golden ratio

**Abstract**—Backpropagation with gradient descent is a common optimization strategy employed by most neural network architectures in machine learning. However, finding optimal hyperparameters to guide training has proven challenging. While it is widely acknowledged that selecting appropriate parameters is crucial for avoiding overfitting and achieving unbiased outcomes, this choice remains largely based on empirical experiments and experience. This paper presents a new probabilistic framework for the learning rate, a key parameter in stochastic gradient descent. The framework develops classic Bayesian statistics into a double-Bayesian decision mechanism involving two antagonistic Bayesian processes. A theoretically optimal learning rate can be derived from these two processes and used for stochastic gradient descent. Experiments across various classification, segmentation, and detection tasks corroborate the practical significance of the theoretically derived learning rate. The paper also discusses the ramifications of the proposed double-Bayesian framework for network training and model performance.

## I. INTRODUCTION

Training neural networks is an art since there is little theoretical guidance, and most hyperparameters are still chosen based on rules of thumb and empirical experiments. Nevertheless, selecting appropriate hyperparameters for training is crucial to avoid overfitting and produce unbiased models that generalize well. This paper presents a theoretical elaboration to enhance our understanding of the training process. Specifically, the paper presents a double-Bayesian framework to explain two hyperparameters that play important roles in stochastic gradient descent (SGD), namely the learning rate and momentum. The paper will derive a theoretically optimal learning rate for SGD, which will be validated through a range of practical grid search experiments for different tasks: handwritten digit classification (MNIST dataset), tuberculosis classification (chest X-rays), lung segmentation (chest X-rays), and malaria parasite detection (blood smear images).

Selecting the appropriate training method, including hyperparameters, significantly influences the trained model and is therefore largely responsible for any bias in model predictions or classification outcomes. Unfortunately, there is no conclusive theory for training neural network weights. For standard

training with gradient descent and backpropagation, which propagate errors backward through the network and adjust weights to minimize errors, a wide range of methods have been proposed. For the rate at which the network’s internal weights need to change at each training iteration, known as the learning rate, only recommendations and rules of thumb exist. Thus, selecting the learning rate is primarily based on empirical experiments or systematic search [1].

Training results can be highly sensitive to the learning rate. For example, a small learning rate slows training and increases the risk of converging to a local optimum. On the other hand, a larger learning rate increases the likelihood that the search will overshoot the minimum loss and exhibit oscillatory behavior. Negotiating this delicate trade-off in regularizing the training process can be time-consuming in practical applications. The literature generally prefers learning rates around 0.01 or smaller for SGD, although reported values vary by several orders of magnitude. For the momentum weight, higher initial values around 0.9 are more common [2], [3], [4], [5]. Many authors have used adaptive learning rates, arguing that the network weights are farthest from their best values at the beginning of the training process, which warrants a larger learning rate [6], [7], [8], [9]. As network weights approach their optimal values, the learning rate can be reduced to reduce the risk of overshooting. Training methods based on adaptive learning rates [6], [7], [8], [9], as well as second-order methods [10], [11], [12], have been tried with varying degrees of success. However, the final verdict is still out on what training method, and in particular, what learning rate, is optimal.

The work in this paper aims to contribute to the ongoing efforts to enhance the performance and interpretability of neural networks. Specifically, the theoretical framework presented aims to improve our understanding of training methods and the concept of optimality in network training. With optimality in mind, the paper is based on a double-Bayesian approach originally described in [13]. This paper presents comprehensive practical validations, building on earlier experiments described in [14], including a comparison of SGD with Adam (Adaptive Moment Estimation) [7], which is widely used in the literature. The paper structure is as follows: Following this introduction, Sections II and III introduce the double-Bayesian decision framework based on which the optimal learning rate is derived. Section IV describes the grid search experiments carried

out for different tasks to evaluate different hyperparameter combinations practically. Section V then presents the results of these experiments. Finally, Section VI and VII summarize the main results and conclusions.

## II. METHODS

The work in this paper is based on a double-Bayesian approach, which involves two dual Bayesian decision processes originally presented in [13]. This section outlines the theoretical foundation of the approach, beginning with a motivation.

### A. Motivation

The motivation for the double-Bayesian optimization approach lies in the inherent uncertainty in measurements. For a random variable with two outcomes,  $A$  and  $B$ , let there be disagreement as to what is  $A$  and what is  $B$ , meaning uncertainty in the probabilities  $P(A)$  and  $P(B)$  of  $A$  and  $B$ . Let these uncertainties be represented by two processes, one trying to estimate  $P(A)$  and the other trying to estimate  $P(B)$ , with  $P(A) = 1 - P(B)$ .

Inherent uncertainty manifests as follows: The process estimating  $P(A)$  cannot know  $P(A)$  for sure, because  $P(A) = 1$  or  $P(A) = 0$  would confirm whether the random outcome is  $A$  or  $B$ , thereby removing the uncertainty. In other words, even if this process estimates  $P(A) = 1$  (or  $P(A) = 0$ ), there is still a chance that  $P(A)$  could be zero (or one). In that case, one can say that the process confuses one and zero. On the other hand, if the process assumes it knows  $P(A) = 1$  (or  $P(A) = 0$ ), it cannot be sure that what it estimates is actually  $P(A)$  because that knowledge would again remove uncertainty as to what is  $A$  and what is  $B$ . The process could actually measure  $P(B)$  and would thus confuse  $A$  with  $B$ . Similar statements hold for the process estimating  $P(B)$ . The knowledge about  $P(A)$  and  $P(B)$  is therefore distributed among the two processes. One process knows what  $A$  and  $B$  are, and the other process knows what zero and one are. The idea is that both processes run in parallel and can correct each other once they have arrived at their estimates.

Based on the above considerations, let both processes interpret  $P(A)$  and  $P(B)$  differently. Without restriction of generality, let the first process interpret  $P(A)$  and  $P(B)$  as follows

$P(A)$ : the certainty in the measurement value of  $A$   
 $P(B)$ : the certainty in the measurement object  $B$ ,

and the second process as

$P(A)$ : the uncertainty in the measurement value of  $A$ , or  
the certainty in the measurement object  $A$ .  
 $P(B)$ : the uncertainty in the measurement object  $B$ , or  
the certainty in the measurement value of  $B$ .

From these definitions, two conditional probabilities can be formulated for each process. For the first process, these probabilities are

$P(A|B)$ : the certainty in the value of  $A$ , when  $B$  is measured.  
 $P(B|A)$ : the certainty in the object  $B$ , when  $A$  is measured.

For the second process, these probabilities are

$P(A|B)$ : the certainty in the object  $A$  when  $B$  is measured.  
 $P(B|A)$ : the certainty in the value of  $B$  when  $A$  is measured.

Note that the first probability of the first process ( $P(A|B)$ ) and the second probability of the second process ( $P(B|A)$ ) are mirrored versions of each other, with  $A$  and  $B$  being swapped. The same can be said about the second probability of the first process and the first probability of the second process.

Each of these conditional probabilities is defined by Bayes' theorem. For example, the first conditional probability of the first process,  $P(A|B)$ , can be written as

$$P(A|B) = P(B|A) * P(A)^* / P(B), \quad (1)$$

where the asterisk indicates a probability estimate of  $P(A)$ , which the first process is trying to estimate. The values for  $P(B)$  and  $P(B|A)$  will be provided by the second process, which estimates  $P(B)$ , using the following Bayes equation:

$$P(B|A) = P(A|B) * P(B)^* / P(A), \quad (2)$$

Here,  $P(B)^*$  stands for the value of  $P(B)$  estimated by the second process, while the values for  $P(A)$  and  $P(A|B)$  are provided by the first process. To make this work, the two processes aim to achieve one objective each as follows:

Objective 1:  $P(A|B) = P(A)^* = P(A)$ , assuming that the second process guarantees  $P(B|A) = P(B)$  (Objective 2).

Objective 2:  $P(B|A) = P(B)^* = P(B)$ , assuming that the first process guarantees  $P(A|B) = P(A)$  (Objective 1).

There is a practical and theoretical motivation for these two objectives: First, the certainty in the value of  $A$ , which is  $P(A)$  for the first process, should be equal to the certainty that the value is indeed the value of  $A$  and not of  $B$ , which is  $P(A|B)$  for the second process. If one certainty is higher than the other, then the higher certainty is not warranted since the minimum certainty in both the measured value and the measured object determines the overall certainty. Second, satisfying  $P(A) = P(A|B)$  meets the requirements for statistical independence, a desired feature because both processes are considered independent. Each process provides unique knowledge about either the measured value or the measured object.

The double-Bayesian model with its two processes involves four parameters  $P(A)$ ,  $P(B)$ ,  $P(A|B)$ , and  $P(B|A)$ . Each process can resolve these unknowns using four equations. For example, the process trying to meet the first objective,  $P(A|B) = P(A)$ , relies on the following three additional equations:

- 1)  $P(A) = 1 - P(B|A)$ , uncertainty principle
- 2)  $P(B) = P(B|A)$ , guaranteed by the co-process
- 3) Bayes' equation

The first equation represents the inverse relationship between the uncertainties of the measured value and the measured object (the uncertainty principle). The larger the former, the smaller the latter, and vice versa. Furthermore, the second process guarantees the second equation, whereas the third

equation is the standard Bayes equation. Similar equations and statements hold for the second process. Double-Bayesian learning intertwines both processes, alternating between them so that the equations will be constantly updated. The idea is that when both processes finally converge, the correct values of  $P(A)$  and  $P(B)$  are found, satisfying  $P(A) = 1 - P(B)$ . The next section will discuss this solving process from the perspective of one of the processes and link it to network training. Before doing so, however, this section will make use of the logarithm to convert probabilities into information (uncertainty) in accordance with information theory [15].

### B. The log-lambda expression

To further formalize the uncertainties in  $P(A)$  and  $P(B)$  in the above motivation, this subsection introduces a  $\log_\lambda$  expression. Let  $\log_b(x)$  be the logarithm for an input  $x$  and a base  $b$ . By definition, the logarithm is the inverse function of taking the power, which leads to the following equation:

$$x = \log_b(b^x) \quad (3)$$

For the base  $b$  of a logarithm, any positive real number can be used so long as  $b \neq 1$ . A logarithm computed for base  $b$  can be converted into a logarithm for base  $b'$  by multiplying it by an appropriate constant, as follows:

$$\log_{b'}(x) = \log_b(x) / \log_b(b') \quad (4)$$

Thus, the logarithm can attain any value for an appropriately chosen base. Specifically, the logarithm can map an input to itself for an appropriately chosen base, defining a fixed point. Mathematically, an input  $x$  to a logarithm is a fixed point if and only if the following equation holds for  $x$ :

$$\log(x) = x \quad (5)$$

Any positive real value  $x$ , except for  $x = 1$ , can be the fixed point of a logarithm if the base  $\lambda$  is chosen appropriately. This statement is a direct consequence of the lemma below.

*Lemma:* For every  $x \in \mathbb{R}^+ \setminus \{1\}$  and  $x' \in \mathbb{R}^+$  there exists a base  $\lambda$  so that  $\log_\lambda(x) = x'$ .

*Proof:* Let  $b \in \mathbb{R}^+ \setminus \{1\}$  be an arbitrary basis for which  $\log_b(x) = y$ . Furthermore, let  $k$  be a multiplier so that  $yk = x'$ . Then,  $\log_\lambda(x) = x'$  for  $\lambda = b^{1/k}$ . This follows from Eq. 4, with  $\log_\lambda(x) = \log_b(x) / \log_b(\lambda) = \log_b(x) / \log_b(b^{1/k}) = \log_b(x) \cdot k = x'$ .  $\square$

The fixed point property of any  $x \in \mathbb{R}^+ \setminus \{1\}$  is a direct consequence of the lemma above, as stated by the following corollary:

*Corollary:* For every  $x \in \mathbb{R}^+ \setminus \{1\}$ , there exists a base  $\lambda$  so that  $\log_\lambda(x) = x$ .

*Proof:* The corollary follows from the above lemma with  $x = x'$ .  $\square$

Using the  $\log_\lambda$  expression, learning can be described as the search for a fixed point corresponding to a target value. With

$$x = \log_\lambda(x) = \log_{\lambda'}(x^*), \quad (6)$$

where  $x^*$  is an estimate of  $x$ , learning consists of finding the appropriate base  $\lambda'$  that maps the input estimate of  $X$ ,

namely  $x^*$ , to  $x$ . Alternatively, Eq. 6 can be written as  $x = \log_{1/\lambda'}(1/x^*)$ , where the reciprocals of  $x^*$  and  $\lambda'$  are used. For simplicity,  $\log_{\lambda'}(x^*)$  will be written as  $\log_\lambda(x)$  for  $x^* = x$ .

The next subsections will connect the  $\log_\lambda$  expression with Bayes' theorem.

### C. Bayes' theorem

Bayes' theorem is a fundamental law in probability theory and is of central importance in machine learning, where it guides the training of machines for decision-making, such as in Bayesian inference or naïve Bayes classification [16], for example. For two events  $A$  and  $B$ , with prior probabilities  $P(A)$  and  $P(B)$ , with  $P(B) \neq 0$  and  $P(B|A) \neq 0$ , Bayes' theorem states the following:

$$\frac{P(A|B)}{P(B|A)} = \frac{P(A)}{P(B)}, \quad (7)$$

where  $P(A|B)$  and  $P(B|A)$  are the conditional or posterior probabilities. Thus,  $P(A|B)$  is the probability of event  $A$  occurring when  $B$  is true, and analogously,  $P(B|A)$  is the probability of  $B$  given that  $A$  is true.

For a machine learning application,  $A$  would be the class of an observed input pattern  $B$ . The probability  $P(A)$  is then the prior probability of class  $A$ , and  $P(B)$  is the prior probability of seeing pattern  $B$ . Consequently,  $P(A|B)$  is the posterior probability of class  $A$  when seeing pattern  $B$ , and  $P(B|A)$  is the posterior probability (or likelihood) of  $B$  within  $A$ . According to Bayes' theorem, three probabilities are needed to compute the probability  $P(A|B)$ :  $P(A)$ ,  $P(B)$ , and  $P(B|A)$ . However, several practical obstacles impede the application of Bayes' theorem. First, no particular method can help determine the prior probability, which is often unknown. Second, the posterior probability is not readily available in most cases and is approximated by assuming a distribution for  $B$  given  $A$ , such as a normal distribution. The double-Bayesian approach incorporates these shortcomings as intrinsic uncertainties.

### D. Double-Bayesian Approach

With only one equation for four parameters, Eq. 7 is underdetermined. Motivated as above, the double-Bayesian approach uses Bayes' theorem and the uncertainty principle to determine two of these parameters [13]. The two remaining parameters will be determined by two Bayesian processes running in parallel, one trying to satisfy  $P(A) = P(A|B)$  and the other trying to satisfy  $P(B) = P(B|A)$ .

With the  $\log_\lambda$  expression, Bayes' theorem can be written as follows:

$$\log_\lambda \left( \frac{P(A|B)}{P(B|A)} \right) = \frac{P(A)}{P(B)} \quad (8)$$

Solving Eq. 8 will be referred to as "solving the *outer Bayes equation*" and will represent one of the two Bayesian processes involved.

The equation for the second process, which will be called *inner Bayes equation*, can be derived from the outer equation by moving the  $\log_\lambda$  expression from the posterior probabilities

to the priors and inverting both the input to the  $\log_\lambda$  expression and its base, resulting in this equation:

$$\log_{1/\lambda} \left( \frac{P(B)}{P(A)} \right) = \frac{P(A|B)}{P(B|A)} \quad (9)$$

The motivation for the name *inner equation* comes from the outer Eq. 8, which can be written as

$$1 = \frac{P(B)}{P(A)} \cdot \log_\lambda \left( \frac{P(A|B)}{P(B|A)} \right) \quad (10)$$

Requiring both factors of the product on the right-hand side (inner part) of this equation to be equal, then leads to the inner equation when the  $\log_\lambda$  expression is moved to the priors, as given by Eq. 9.

### III. SOLVING THE INNER AND OUTER BAYES EQUATIONS

Writing the outer Eq. 10 in the following form facilitates some key observations that will help represent its possible solutions:

$$P(A) = P(B) \cdot \log_\lambda \left( \frac{P(A|B)}{P(B|A)} \right) \quad (11)$$

The input to the  $\log_\lambda$  expression can be considered the input to this equation, whereas the value on the left-hand side of the equal sign,  $P(A)$  in this case, can play the role of a teaching input. Learning then consists of finding an appropriate base  $\lambda$  so that Eq. 11 is met. Assuming the teaching input to be invariable,  $P(A)$  can be replaced by any constant, as the base can be adjusted accordingly.

#### A. Golden Ratio

The first observation is about the inner equation, which is satisfied when both product terms on the right-hand side of Eq. 11 become equal. This is the case when

$$P(B) = \frac{P(A|B)}{P(B|A)} = \frac{1 - P(B)}{P(B)}, \quad (12)$$

which applies the two learning goals  $P(A|B) = 1 - P(B|A)$  and  $P(B) = P(B|A)$ . Therefore, Eq. 12 is satisfied when  $P(B)$  equals the golden ratio [17], [13], [18]. The golden ratio will be denoted by  $\varphi \approx 0.62$  in the following. Note that the literature very often uses  $\varphi \approx 1.62$  as the value for the golden ratio, which is the reciprocal of the value used here. More details about the equations defining the golden ratio, including its multiple values and their complements, are given in [13].

#### B. Pythagorean Identity

The second observation is again about the inner equation, when the terms  $1 - P(B)$  and  $P(B)$  are used for the numerator

and denominator in the  $\log_\lambda$  expression of Eq. 11, which leads to the following sequence of transformations:

$$P(B) = \log_\lambda \left( \frac{1 - P(B)}{P(B)} \right) \quad (13)$$

$$= \log_\lambda \left( 1 - P(B)^2 \right) \quad (14)$$

$$= 2 \cdot \log_\lambda \left( \sqrt{1 - P(B)^2} \right) \quad (15)$$

$$= \log_\lambda \left( \cos(\phi) \right) \quad (16)$$

Note that each of these equations can be satisfied with an appropriate, albeit different  $\lambda$  that can vary among them. Eq. 14 can be obtained from Eq. 13 by first bringing the denominator,  $P(B)$ , to the left-hand side of the equation and then using  $P(B)^2 = 1 - P(B)$ . Eq. 15 exploits the logarithmic rule  $\log(x^c) = c \cdot \log(x)$ , which holds for any constant  $c$ . Finally, Eq. 16 can be written with trigonometric functions for an angle  $\phi \in [0; \pi/2]$ , as shown in Eq. 16, which exploits the Pythagorean relationship between sine and cosine:  $\sin^2(\phi) + \cos^2(\phi) = 1$ . In addition, the factor 2 has been incorporated into the base  $\lambda$ . The probability  $P(B)$  on the left-hand side of Eq. 16 will then be equal to  $\sin(\phi)$ .

With both factors on the right-hand side of Eq. 11 described by sine and cosine, the outer equation can be written as

$$P(A) = \sin(\phi) \cdot \log_\lambda \left( \cos(\phi) \right) \quad (17)$$

Solutions to the inner and outer Bayes equations are then points on the unit circle defined by an angle  $\phi$ . For example, the outer Bayes equation is satisfied for  $\phi = 0$  and  $\phi = \pi/2$ . For  $\phi = 0$ ,  $\log_\lambda(\cos(\phi))$  and  $\sin(\phi)$  will be 0, and consequently,  $P(A)$  will be zero. For  $\phi = \pi/2$ ,  $\log_\lambda(\cos(\phi))$  will be infinity for any given  $\lambda$  and  $\sin(\phi)$  will be 1, which means that  $P(A)$  will be infinity. Note that when  $P(A)$  becomes larger than 1, taking the reciprocal of all terms, including the basis  $\lambda$ , would keep the value between 0 and 1. In any case,  $\phi = 0$  or  $\phi = \pi/2$ , the  $\log_\lambda$  expression will be equal to  $P(A)$  on the left-hand side of Eq. 17, satisfying the outer Bayes equation. For  $\phi = \pi/4$ , on the other hand, the two terms on the right-hand side of Eq. 17,  $\sin(\phi)$  and  $\cos(\phi)$ , are equal to  $1/\sqrt{2}$ , satisfying the inner Bayes equation.

#### C. Intrinsic Uncertainty

As outlined above, the outer and inner Bayes equations stand for two processes that compute complementary information. If one of the equations is met, then solving the other faces maximum uncertainty. Since the outer Bayes equation is satisfied for  $\phi = 0$  or  $\phi = \pi/2$ , as derived in the previous subsection, the inner Bayes equation needs to be satisfied for  $\phi = \pi/4$ , which is the angle in the middle of  $\phi = 0$  and  $\phi = \pi/2$ .

Let the angle  $\phi$  represent the uncertainty in the measurement value for the motivational measurement example above, and  $\lambda$  represent the uncertainty in what is actually measured,  $A$  or  $B$ , then the intrinsic uncertainty translates as follows: The more is known about  $\phi$ , the less is known about  $\lambda$ ; and vice versa, the more is known about  $\lambda$ , the less is known about  $\phi$ . When

the outer Bayes equation is satisfied for  $\phi = 0$  or  $\phi = \pi/2$ , the base parameter  $\lambda$  that can be used to satisfy the inner equation is uncertain. It could be  $\lambda$  or  $1/\lambda$ , depending on whether  $A$  is indeed  $A$  or  $B$ . If  $A$  is actually  $B$ , then the fraction in the  $\log_\lambda$  expression of Eq. 11 needs to be inverted, which means changing the sign of the logarithm, which in turn is equivalent to inverting the base  $\lambda$ . On the other hand, when the inner equation is satisfied, the true value of  $\phi$  is unknown. It could be  $\phi = 0$  or  $\phi = \pi/2$ .

To satisfy the inner equation at  $\phi = \pi/4$ ,  $P(B)$  needs to match the golden ratio according to Eq. 12. However, this result was derived from Eq. 11 for  $P(A) = 1$ . For  $P(A) = \sqrt{2}$ , as would be consistent with  $\phi = \pi/4$ ,  $P(B)$  becomes a multiplier for the gradient of the outer equation. Because  $P(B)/\sqrt{2}$  needs to match  $\varphi$  so that the inner Bayes equation is met, the value of  $P(B)$  follows with

$$P(B) = \sqrt{2} \cdot \varphi = \alpha \approx 0.874 \quad (18)$$

Eq. 18 assigns this value to the variable  $\alpha$  because of its importance in neural network training, where it serves as the momentum weight (see below).

A similar parameter  $\eta$  can be derived based on the dual process, starting from Eq. 11, by first replacing  $A$  with  $B$ , and then moving the logarithm from the posterior to the prior probabilities. Following these steps leads to this equation:

$$P(A|B) = P(B|A) \cdot \log_\lambda \left( \frac{P(A)}{P(B)} \right) \quad (19)$$

Here,  $P(B|A)$  plays the role of the multiplying constant. Accordingly, the parameter  $\eta$  can be computed from  $\alpha$  by following the same steps, which leads to a value that will serve as the learning rate for neural network training:

$$\eta = (1 - \alpha)^2 \approx 0.016 \quad (20)$$

Note that the value of  $P(B|A)$  needs to be squared because it was taken out of the  $\log_\lambda$  expression in which values are roots as per Eq. 15.

The next subsection explains why  $\eta$  and  $\alpha$  can serve as the learning rate and momentum weight in stochastic gradient descent for network training.

#### D. Double-Bayesian Training

The primary goal of a supervised learning method for neural networks is to ensure that the network’s output matches its teaching input. A training method based on stochastic gradient descent (SGD) and backpropagation computes the gradient of a loss function with respect to each network weight, where the loss function measures the difference between the network’s output and the teaching input. In a backpropagation step, the method minimizes the loss by following the gradient and updating the network weights accordingly [19]. Weights are updated one network layer at a time, iteratively backpropagating the gradient from the output layer to the input layer. To move along the gradient towards the minimum of the loss function, a delta is added to each weight, which has the following form and can include a momentum term:

$$\Delta w_{ij}(t) = -\eta \frac{\partial L}{\partial w_{ij}(t)} + \alpha \cdot \Delta w_{ij}(t-1) \quad (21)$$

In Eq. 21,  $L$  stands for the loss function, and  $\Delta w_{ij}(t)$  denotes the delta added to each weight  $w_{ij}$  between node  $i$  and node  $j$  of the network at training iteration (or time)  $t$ . The term  $\partial L / \partial w_{ij}(t)$  is the partial derivative of the loss function with respect to  $w_{ij}$ , at time  $t$ , which is multiplied by the learning rate  $\eta$ . The sign of  $\Delta w_{ij}(t)$  is negative so that the loss function approaches its minimum. In practice, a momentum term describing the change in weight at time  $t-1$ ,  $\Delta w_{ij}(t-1)$ , is commonly added. This term is typically multiplied by a weighting factor  $\alpha$ , as seen in Eq. 21, which is the momentum weight.

The values of the momentum weight  $\alpha$  and the learning rate  $\eta$  are usually determined empirically using rules of thumb, a practice further confirmed by the references cited in the discussion below. However, this paper argues that the theoretically derived values from above should be used for the learning rate ( $\eta \approx 0.016$ ) and momentum term ( $\alpha \approx 0.874$ ). The reasoning is that the teaching input and the network output can be treated as intrinsic uncertainties about a measurement object and its measurement, similar to the motivational example at the beginning of this paper. The uncertainties can be represented by two parameters (e.g.,  $P(A)$  and  $P(A|B)$ ) and resolved by two processes based on the inner and outer Bayes equations, where one process tries to make them equal by adjusting  $\lambda$ .

Each of the inner and outer Bayes equations determines one variable needed to solve the Bayes equation. However, only one of the equations can be solved at a given time - the closer to solving one equation, the further away from solving the other, depending on the angle  $\phi$ . The point furthest away from solving the outer equation is reached for  $\phi = \pi/4$ , when the inner equation must be satisfied. Considering the  $\log_\lambda$  expression as input, the parameter  $\alpha$  is a multiplying constant for the gradient of the outer equation. Assuming that the outer equation defines  $P(A) = P(A|B)$  as a prerequisite for the inner equation, without restriction of generality, the factor  $\alpha$  can be used as the momentum weight for time  $t-1$ . On the other hand, the factor  $\eta$  derived above for the dual process can be used as the learning rate for the current iteration at time  $t$ .

In light of these results, the inner and outer Bayes equations can serve as a generic model for making a network output equal to its teaching input. Training involves switching between two processes: one for satisfying the inner Bayes equation and one for *not* satisfying the outer Bayes equation. This alternating procedure ensures that the uncertainty about one variable is minimized while maximizing that of its counterpart, since it is not possible to know both with absolute certainty.

The actual loss function used to measure the difference between the network output and the teaching input plays a minor role in this context, as its derivative will be included in the overall gradient computation and multiplied using the chain rule, which can be “absorbed” by the base parameter  $\lambda$ .

## IV. EXPERIMENTS

The experiments reported below constitute a comprehensive performance evaluation of the theoretically derived learning rate ( $\eta = 0.016$ ). A systematic grid search over a wide range of values for  $\eta$  highlights their relative performance differences.

Specifically, the experiments used six values for  $\eta$ : 0.0001, 0.001, 0.01, 0.016, 0.1, and 0.2. These values included the theoretical value derived above ( $\eta \approx 0.016$ ) and other values that were either close to the derived value or had been successfully used in the literature, ranging from very low (0.0001) to relatively high (0.2). All learning rate values were fixed throughout training. Additionally, ten momentum values were used in the experiments: 0.0, 0.2, 0.4, 0.6, 0.8, 0.825, 0.85, 0.874, 0.9, and 0.925. These values spanned an interval from 0 to 1, with higher resolution near the theoretically derived value of 0.874. Thus, all possible combinations of hyperparameter values spanned a  $6 \times 10$  grid. This large number of values was chosen to investigate the overall performance of different hyperparameter combinations across various applications. In addition to SGD with momentum, the Adam optimizer was used for comparison, with its  $\beta_1$  parameter serving as the momentum and  $\beta_2$  set to 0.999 for all experiments [7].

The experiments were conducted on four different tasks: 1) classification of handwritten numerical digit images using a customized convolutional neural network, 2) classification of chest X-ray images for tuberculosis detection using the DenseNet121 architecture [20], 3) semantic segmentation of the lung region in chest X-ray images using the YOLOv8m-seg network [21], and 4) detection of cells in microscopy images of thin blood smears using the YOLOv8m network. Fig. 1 shows example images from the different datasets used in the experiments. For each task, the performance of SGD and Adam was systematically evaluated across varying training set sizes and noise levels. First, a baseline comparison was performed with the entire training set for each optimizer. To further explore their performance under simulated scarcity of training data, the training set was reduced to 75%, 50%, and 25% of its original size. This reduction in training set size allowed observing how an optimizer performed under varying amounts of training data, assuming that providing less training data poses a harder problem. In addition to varying training set sizes, the impact of noise was examined by applying different levels of noise. A noise level is defined as the percentage of randomly inverted pixel intensities, where an inverted intensity is computed as 255 minus its original value. Noise was applied solely to the test set, leaving the training and validation sets untouched. The goal of including noise during testing was to measure the generalization performance and noise resilience of the models trained with SGD and Adam. Experiments for each task were repeated 5 times with different random seeds to account for variability introduced by randomness. The average performance across these five runs was reported to provide a more robust and reliable measure of each model’s performance.

#### A. Handwritten Digit Classification

A deep learning model based on an 11-layer convolutional neural network (CNN) was trained for handwritten digit classification using the MNIST database [22]. The CNN model began with a convolutional layer that took a single-channel input (a grayscale image) and applied 16 filters, followed by a second convolutional layer that expanded the channel size

to 32. Both convolutional layers used a kernel size of  $3 \times 3$ , a stride of 1, and a padding of 1. After each convolution, a ReLU activation function introduced non-linearity, and a max pooling operation with a  $2 \times 2$  kernel and stride reduced the spatial dimensions by half. A dropout layer with a rate of 0.25 was applied after flattening the output to prevent overfitting. The network was concluded with two fully connected layers, yielding a final output of 10 classes, with the maximum output value determining the class of an input image. Around two hundred thousand parameters were used for an input image size of  $28 \times 28$ . Model weight initialization was performed using the Kaiming uniform method [23]. No data augmentation techniques were applied. The input was normalized to the  $[-1; 1]$  range, and training was conducted over 100 epochs with a batch size of 64, using cross-entropy as the loss function. Sizes of the training, validation, and test sets were 54,000, 6,000, and 10,000, respectively. Model performance was assessed using five-fold cross-validation.

#### B. Tuberculosis Classification

For this task, tuberculosis (TB) and non-TB cases were classified using chest X-ray (CXR) images from the TBX11K dataset [24], [25]. This set contains 11,200 frontal CXRs, including 800 TB cases, from multiple hospitals in China. A model was trained on the 800 TB images and on randomly selected non-TB CXR images. All images had an intensity range of  $[0; 255]$  and were standardized to a size of  $512 \times 512$  pixels.

DenseNet121 [20] was initialized with ImageNet pre-trained weights. Images were resampled to  $256 \times 256$ , with intensities scaled to  $[0; 1]$  and then normalized using channel means ( $[0.485, 0.456, 0.406]$ ) and standard deviations ( $[0.229, 0.224, 0.225]$ ). Data augmentation included random cropping to  $150 \times 150$  patches. Training was performed over 100 epochs with a batch size of 64, using cross-entropy as the loss function. The training, validation, and test sets comprised 1,024, 256, and 320 images, respectively. Model performance was evaluated using 5-fold cross-validation, with standard accuracy serving as the metric for TB/non-TB classification.

#### C. Semantic Lung Segmentation

This task involved lung segmentation on CXR images for a COVID-19 dataset [26], comprising a training set of 2,963 images, a validation set of 977 images, and a separate test set of 1,301 images. The YOLOv8-seg architecture was used to segment the lung regions [21]. YOLOv8-seg offers five variants corresponding to different model sizes, ranging from nano (n) to extra large (x): YOLOv8(n), YOLOv8(s), YOLOv8(m), YOLOv8(l), and YOLOv8(x). The YOLOv8(m) variant was selected to balance training time and performance. COCO pre-trained weights were used for model initialization [27]. Images were resampled to  $640 \times 640$ , with intensities scaled to  $[0; 1]$ . Data augmentation was applied using YOLOv8’s default settings, including 10% translation, 50% scaling, random left-right flipping, and mosaic augmentation. The training used auto mode for batch size, allocating 60% of GPU memory (batch=-1), resulting in a batch size of 23 on a V100 GPU and

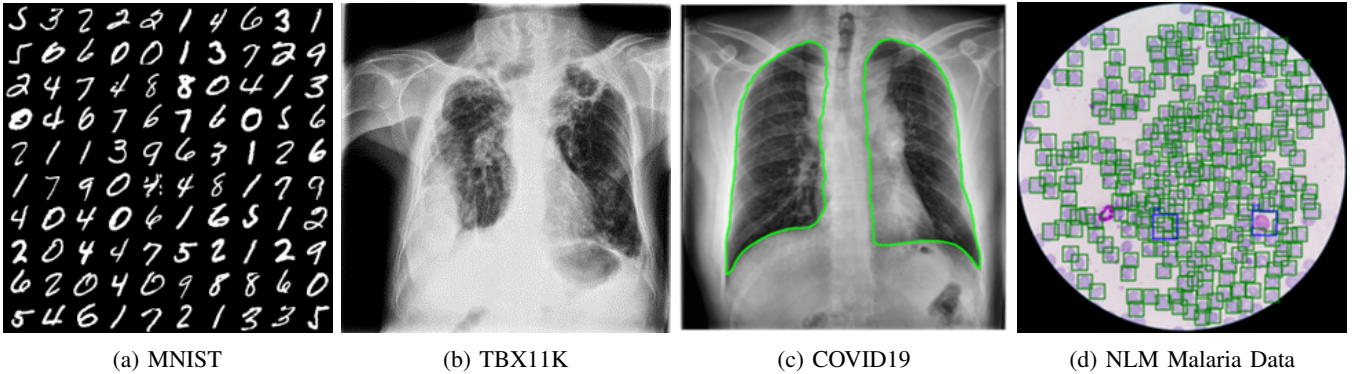


Fig. 1: Images used in this study include (a) handwritten digits (MNIST), (b) frontal chest X-rays with TB/not-TB labels (TBX11K), (c) frontal chest X-rays with manual ground-truth lung segmentations (COVID19), and (d) blood smear images annotated with boxes around malaria-infected and uninfected cells.

58 on an A100 GPU. Training was conducted for 100 epochs with early stopping. The final segmentation was obtained by retaining only the two largest objects in the prediction mask. This step helped eliminate smaller objects that were considered outliers, as the lung typically consists of two large structures representing the left and right lungs. The performance of SGD and Adam was evaluated based on the intersection over union (IoU) metric.

#### D. Malaria Cell Detection

For this task, a YOLOv8(m) was trained to detect *Plasmodium falciparum* (*P. falciparum*) and *Plasmodium vivax* (*P. vivax*), the two most common malaria parasite species, in thin blood smear images [28], [29], [21]. In particular, the models were trained and evaluated using a dataset of 364 malaria cases in Bangladesh, comprising 3,532 images containing 7,952 instances of red blood cells (RBCs) infected with *P. falciparum*, 4,346 RBCs infected with *P. vivax*, and over 860,000 uninfected RBCs. The YOLOv8(m) model was initialized using COCO weights. Images were resampled to  $1024 \times 1024$ , with intensities scaled to  $[0; 1]$ . Data augmentation was applied using the default settings in YOLOv8, including 10% translation, 50% scaling, random left-right flipping, and mosaic augmentation.

Training was conducted using a batch size of eight and spanned 300 epochs. The experiments compared SGD and Adam across varying training set sizes to analyze their generalization performance and dependence on training data. Furthermore, the experiments evaluated the performance under noise to investigate the robustness of the trained models. These experiments were done by applying various noise levels to the test set. All images were first converted from the RGB color space to the HSI (Hue, Saturation, Intensity) color space. In HSI, hue and saturation represent a color, while intensity represents its brightness. Noise is added to the intensity channel before converting the images back to RGB color. This method allows noise to affect brightness without affecting the image’s color information. The HSI approach was chosen because it is consistent with previous tasks that introduced noise into grayscale images, which carry only brightness information.

The mean average precision at 50% IoU (mAP50) was used for evaluation [30], [27]. This performance measure considers precision and recall across different confidence thresholds and is particularly useful for assessing object detection tasks.

## V. RESULTS

This section summarizes the results of the experiments, starting with the systematic grid search experiments for learning rate and momentum. Fig. 2 shows the model accuracies for each task and for all combinations of learning rate and momentum weight when models are trained with SGD. For each task, the accuracies of the top 10 models are highlighted in green boxes, with the best overall performance shown in red. Note that the best performance may be achieved with different pairs of learning rate and momentum values. Fig. 2 shows that the theoretically predicted learning rate ( $\eta \approx 0.016$ ) performs better than other learning rates for handwritten digit classification, TB classification, and malaria cell detection. Moreover, most of the ten best-performing models for these tasks were trained with a learning rate of 0.01 or 0.016, and thus with either the theoretically predicted learning rate or a rate very close to it. For the lung segmentation task, the best learning rates span a wider range. Nevertheless, the theoretical learning rate was in the top 10, and the best-performing model was trained with a learning rate very close to the predicted value (0.01). For handwritten digit classification and TB classification, a Wilcoxon signed-rank test was used to evaluate the performance of the proposed learning rate and momentum pair (0.016, 0.874) against all other pairs in the top 10 performers. The results indicated no statistically significant difference between the proposed pair and the others in the top 10 ( $p > 0.05$ ), suggesting that no other pair of learning rate and momentum performs better than the proposed pair (0.016, 0.874).

To corroborate these results and investigate any potential relationship with training set size, grid searches for all tasks were repeated with training set sizes of 75%, 50%, and 25% of the original size. Table I shows the best-performing learning rates for these experiments, including the results above for the original training set. The results show that the theoretical

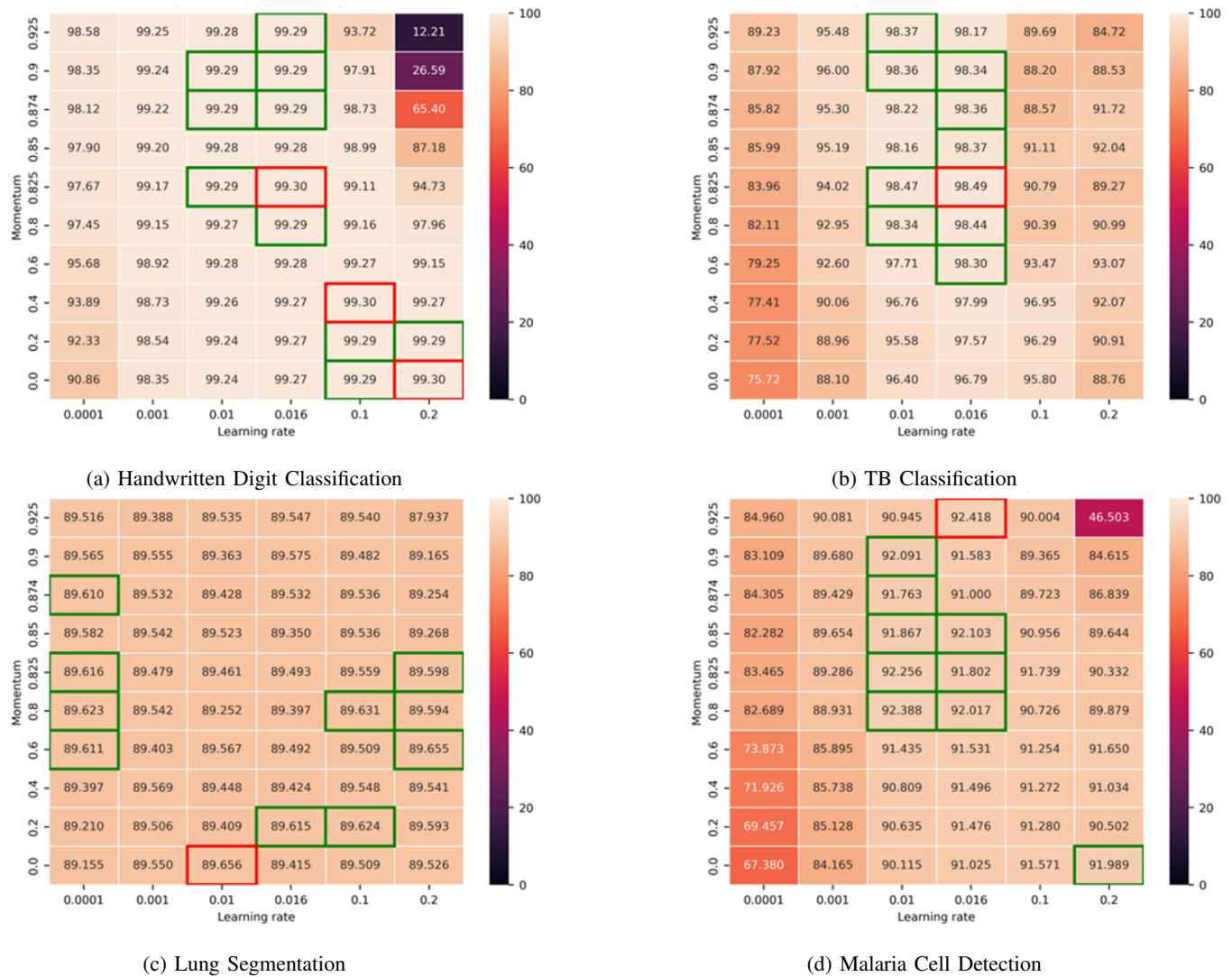


Fig. 2: Grid search results for each task using SGD with 100% of the training data. The top 10 performing models are highlighted in green boxes, while the best overall performance is marked in red. The standard deviation (std) of the top 10 values was calculated for each task. In handwritten digit classification, std ranged from 0.02 to 0.03; for TB classification, the range was 0.13 to 0.46; in lung segmentation, the range was 0 to 0.02; and for malaria cell detection, std ranged from 0.30 to 1.25. The standard deviation was generally low for all tasks, indicating a high degree of consistency among the top values. Note that the performance measure is task specific: (a) and (b) used accuracy, (c) used intersection over union, and (d) used the mAP50 score.

learning rate performed best across all training set sizes for handwritten digit classification, TB classification, and malaria cell detection, except for handwritten digit classification with 75% training data, where it was second-best. For lung segmentation, the theoretical learning rate was in the top 7 most of the time, and the close 0.01 rate was either the best or in the top 4.

#### A. Comparison of SGD and Adam

Several grid search experiments were conducted to compare the performance of SGD and Adam across model accuracy, noise robustness, and convergence rate. The following subsections summarize the results.

1) *Performance*: Table II compares the performances of SGD and Adam. It lists the average performance of the top 10 models for each optimizer, task, and training set size. For the classification tasks (digits and TB), performance was measured as classification accuracy. In contrast, for lung segmentation and malaria cell detection, performance was measured as IoU and mAP50, respectively. The values in bold indicate the highest average performance for each training set size. Table II shows that SGD slightly but consistently outperformed Adam, except for one grid search experiment in TB classification. As the training set size decreased, the performance of both optimizers degraded, as expected, with no significant differences in behavior.

TABLE I: The best SGD learning rates for each task and different training set sizes according to the grid search. The theoretically derived learning rate (0.016) and rates close to it (0.01) are highlighted in bold.

Task	Training Size	Best Learning Rate
MNIST	100%	<b>0.016</b> , 0.1, 0.2
	75%	0.1 (0.016: top-2)
	50%	<b>0.016</b> , 0.2
	25%	<b>0.016</b> , 0.1
TB Classification	100%	<b>0.016</b>
	75%	<b>0.016</b>
	50%	<b>0.016</b>
	25%	<b>0.016</b>
Lung Segmentation	100%	<b>0.01</b> (0.016: top-7)
	75%	0.001 (0.016: top-2)
	50%	<b>0.01</b> (0.016: top-4)
	25%	0.0001 (0.01: top-4)
Malaria Cell Detection	100%	<b>0.016</b>
	75%	<b>0.016</b>
	50%	<b>0.016</b>
	25%	<b>0.016</b>

Table III compares the loss and accuracy of the best-performing models for SGD and Adam. The best model was selected based on the minimum overall validation set loss achieved during grid search. Note that Table III shows the performance of the best model, whereas Table II shows the average performance of the top 10 models. According to Table III, the best model trained with SGD almost consistently outperformed the best model trained with Adam, except for two cases. In six cases, the best-performing model trained with Adam achieved the lowest validation-set loss but not the best test-set performance. On the other hand, there was only one case in which SGD achieved the lowest loss but not the highest performance. This observation indicated that Adam was more prone to overfitting. Both optimizers again demonstrated similar performance stability as the training set size decreased.

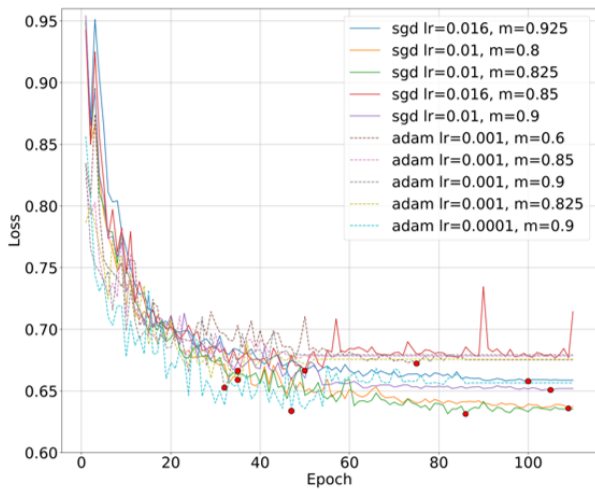
2) *Convergence*: Fig. 3 shows the convergence behavior of SGD and Adam for the malaria cell detection task. Specifically, it shows the validation loss of the top 5 models for each optimizer. The validation loss of each model for all epochs is shown on the left-hand side of Fig. 3. The left-hand side also displays the minimum validation-set loss for each model, ranked by mAP50, along with the learning rate and momentum for each model. In addition, the last column in the table on the right-hand side of Fig. 3 lists the number of epochs after which the minimum loss was achieved during training. SGD achieved its lowest loss with the proposed learning rate (0.016), and the next-best models trained with SGD achieved their lowest

TABLE II: Average performance of the top 10 models using SGD and Adam optimizers across various tasks and training set sizes (100%, 75%, 50%, 25%). Metrics are reported as mean  $\pm$  standard deviation, using accuracy for handwritten digits and TB classification tasks, IoU for lung segmentation, and mAP50 for malaria cell detection. Bold values highlight the highest average performance for each task. Results marked with an asterisk are significantly better ( $p < 0.05$ , Wilcoxon signed-rank test).

Task	Training Size	SGD (Avg top-10)	Adam (Avg top-10)
MNIST (Accuracy)	100%	<b>99.29 <math>\pm</math> 0.00*</b>	99.24 $\pm$ 0.01
	75%	<b>99.24 <math>\pm</math> 0.01*</b>	99.17 $\pm$ 0.01
	50%	<b>99.10 <math>\pm</math> 0.01*</b>	99.02 $\pm$ 0.01
	25%	<b>98.79 <math>\pm</math> 0.01*</b>	98.69 $\pm$ 0.01
TB Classification (Accuracy)	100%	98.38 $\pm$ 0.06	<b>98.51 <math>\pm</math> 0.10*</b>
	75%	<b>97.98 <math>\pm</math> 0.12*</b>	97.78 $\pm$ 0.06
	50%	<b>96.83 <math>\pm</math> 0.34*</b>	96.39 $\pm$ 0.15
	25%	<b>90.49 <math>\pm</math> 0.88</b>	90.48 $\pm$ 0.62
Lung Segmentation (IoU)	100%	<b>89.62 <math>\pm</math> 0.02*</b>	89.57 $\pm$ 0.05
	75%	<b>89.59 <math>\pm</math> 0.04*</b>	89.51 $\pm$ 0.03
	50%	<b>89.56 <math>\pm</math> 0.04*</b>	89.41 $\pm$ 0.05
	25%	<b>89.37 <math>\pm</math> 0.03*</b>	89.15 $\pm$ 0.06
Malaria Cell Detection (mAP50)	100%	<b>92.07 <math>\pm</math> 0.22*</b>	91.08 $\pm$ 0.36
	75%	<b>91.85 <math>\pm</math> 0.19*</b>	91.30 $\pm$ 0.18
	50%	<b>90.42 <math>\pm</math> 0.20*</b>	90.20 $\pm$ 0.23
	25%	<b>87.27 <math>\pm</math> 0.59</b>	87.15 $\pm$ 0.32

losses at either the same or a very close learning rate. Adam performed best for the commonly used, small learning rate of 0.001. While SGD achieved the best overall performance, validation losses did not differ substantially among optimizers. However, there was a striking difference in the number of epochs needed to reach the minimum loss. Adam reached its minimum loss much earlier and could be roughly two to three times faster than SGD. This also becomes evident on the left-hand side of Fig. 3, which shows the validation loss over time for models trained with SGD and Adam, with red dots indicating the minimum loss. These results suggest that Adam’s faster convergence may be the primary reason for its popularity, rather than an elusive performance advantage.

3) *Stability under noise*: Another experiment compared the robustness of SGD and Adam on noisy test data. Fig. 4 shows the performance of both optimizers for each task under noisy conditions, where a certain percentage of pixels were randomly flipped in each image of the test data. The errors reported in Fig. 4 are the mean errors of the top 10 models identified in the grid search experiments. The individual errors are the complements of the respective performance measures used for each task (accuracy, IoU, mAP50). Error rates of SGD are represented by green bars, and Adam’s error rates



(a)

Optimizer	(Learning rate, momentum)	mAP50	Min Validation Loss	Epochs
SGD	(0.016, 0.925)	<b>92.42±0.64</b>	0.66	100
	(0.01, 0.8)	92.39±1.11	0.64	109
	(0.01, 0.825)	92.26±0.93	<b>0.63</b>	86
	(0.016, 0.85)	92.10±1.10	0.67	50
	(0.01, 0.9)	92.09±0.86	0.65	105
Adam	(0.001, 0.6)	<b>91.76±0.34</b>	0.67	75
	(0.001, 0.85)	91.63±1.10	0.67	35
	(0.001, 0.9)	91.31±0.60	0.65	32
	(0.001, 0.825)	91.25±0.82	0.66	35
	(0.0001, 0.9)	90.92±1.34	<b>0.63</b>	47

(b)

Fig. 3: (a) Convergence speed of the top 5 performing models for malaria cell detection, ranked by mAP50, with solid lines representing SGD and dashed lines representing Adam. Red dots indicate the epoch at which each model achieves its minimum validation loss. (b) Comparison of mAP50, minimum validation loss, and the number of epochs required to reach the minimum validation loss for each model. The highest mAP50 values and lowest validation losses are highlighted in bold for SGD and Adam, respectively.

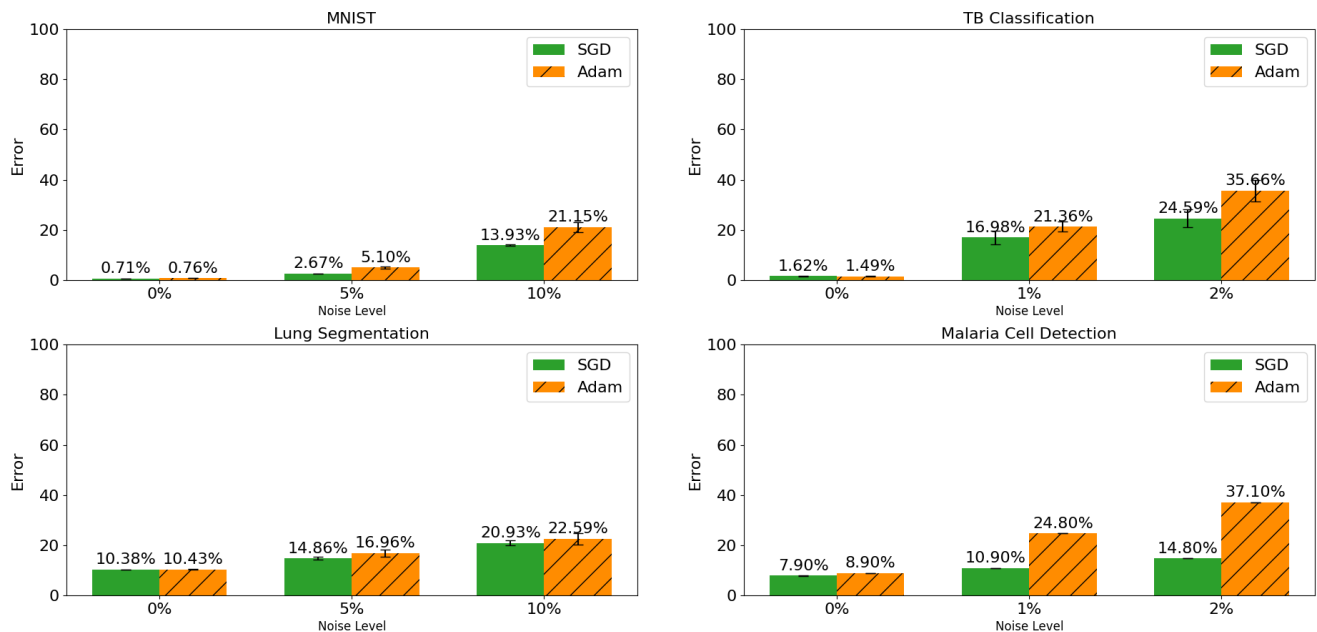


Fig. 4: Errors of SGD (green) and Adam (hatched orange) for different tasks and noise levels: (a) handwritten digit classification (MNIST), (b) TB classification, (c) lung segmentation, and (d) malaria cell detection. Errors are averaged across the top 10 performing models from an extensive grid search over different learning rates and momentum values. The complements of accuracy (digits and TB classification), IoU (lung segmentation), and mAP50 (cell detection) are used as error measures. Noise levels are calculated as the percentage of pixels randomly flipped in each test image.

are represented by hatched orange bars. In addition to the baseline results with 0% noise, Fig. 4 shows the results for two noise levels for each task: 5% and 10% for handwritten digit classification and lung segmentation, and 1% and 2%

for TB classification and malaria cell detection. Fig. 4 shows that under noisy conditions, the error of SGD was always lower than the error of Adam. The only case in which Adam performed slightly better than SGD was the baseline TB

TABLE III: Comparison of minimum validation loss and accuracy for different tasks across varying training set sizes (100%, 75%, 50%, 25%) using SGD and Adam optimizers. The results pertain to the best-performing models for each optimizer, with the loss and accuracy values reported. The bold values indicate the lowest loss or highest accuracy for each task and training size.

Task	Training Size	SGD	Adam
		(Best model) Loss / Accuracy	(Best model) Loss / Accuracy
MNIST	100%	0.031 / <b>99.30</b>	<b>0.030</b> / 99.25
	75%	<b>0.017</b> / <b>99.26</b>	0.019 / 99.19
	50%	<b>0.027</b> / <b>99.12</b>	0.029 / 99.05
	25%	<b>0.045</b> / <b>98.81</b>	0.047 / 98.71
TB Classification	100%	0.089 / 98.49	<b>0.066</b> / <b>98.64</b>
	75%	0.045 / <b>98.21</b>	<b>0.041</b> / 97.84
	50%	0.221 / <b>97.17</b>	<b>0.106</b> / 96.72
	25%	0.423 / <b>92.03</b>	<b>0.307</b> / 91.82
Lung Segmentation	100%	<b>0.61</b> / 89.66	0.62 / <b>89.67</b>
	75%	<b>0.61</b> / <b>89.72</b>	0.62 / 89.58
	50%	<b>0.63</b> / <b>89.62</b>	0.64 / 89.48
	25%	<b>0.62</b> / <b>89.42</b>	0.65 / 89.24
Malaria Cell Detection	100%	<b>0.66</b> / <b>92.42</b>	0.67 / 91.76
	75%	<b>0.69</b> / <b>92.18</b>	0.70 / 91.61
	50%	0.72 / <b>90.71</b>	<b>0.68</b> / 90.68
	25%	0.76 / <b>88.36</b>	<b>0.72</b> / 87.89

classification experiment with no noise. Furthermore, the error gap between SGD and Adam widened at higher noise levels in almost all cases. Although not shown in Fig. 4, this trend continued when noise was increased to even higher levels. These findings suggest that models trained with SGD are more robust to noise than those trained with the Adam optimizer.

## VI. DISCUSSION

The literature lacks a theoretical approach that provides a definitive answer to the question of which optimization strategy to use for neural network training, including well-defined optimal hyperparameters. There also exists no comprehensive practical evaluation of different optimization strategies and hyperparameters. One reason is the high costs of running extensive grid search experiments. For example, the experiments in this paper required a runtime of roughly 40,000 hours on a mix of NVIDIA@V100 and A100 GPUs. Therefore, following current trends and applying rules of thumb has been standard practice in the literature.

This paper presents a theoretical approach to neural network training and provides a thorough practical evaluation of two optimizers, SGD and Adam. Specifically, the theoretical model views training as a double-Bayesian process and supports the use of SGD with two key hyperparameters: the learning rate and the momentum weight. The traditional understanding is that the momentum term in SGD optimizers improves stochastic gradient descent by dampening oscillations. However, the

dual-process model offers an alternative explanation for the performance improvement attributable to the momentum term. To date, a conclusive theory for determining the optimal values of the learning rate  $\eta$  and the momentum weight  $\alpha$  has been lacking. As mentioned in the introduction, experiments with adaptive methods [6], [7], [8], [9] and second-order methods [10], [11], [12] did not lead to an ultimate answer. Both parameters are usually determined heuristically through empirical experiments or systematic search [1]. Training can be highly sensitive to the learning rate, either failing to reach a global minimum or overshooting it. The literature arguably prefers learning rates around 0.01 for SGD, whereas higher values around 0.9 are preferred for the momentum weight [2], [3], [4], [5].

Regarding stability under noise, Subhajt et al. investigated the training of neural network models on datasets corrupted with noise, employing a range of different optimizers [31]. They aimed to understand how various optimizers respond to noisy data during training. They evaluated the trained models on clean data to assess and benchmark the extent to which the optimizers might overfit, given the noise in the training set. Their results demonstrated the robustness of SGD relative to adaptive optimization methods such as Adam and RMSProp under noisy training data.

The experimental results reported in Section V thoroughly explored various settings for learning rate and momentum across multiple tasks and datasets, thereby broadening and enhancing the applicability of the findings. The experiments confirm the values commonly used in the literature and predicted by the proposed double-Bayesian approach. They also support the observation in [31] that SGD displays a superior generalization performance in noisy conditions, whereas Adam seems more prone to over-fitting. As shown in Fig. 3, Adam consistently performed best for very small learning rates, smaller than the best rates observed for SGD. On the other hand, the momentum appeared to have no significant impact on Adam’s performance. For SGD, higher momentum values yielded the best performance, ranging from 0.4 to 0.8 and above.

In summary, the experiments corroborate the values suggested for SGD in [13], [17], namely a learning rate of about 0.016 and a momentum weight of 0.874. Moreover, the experiments show that, when optimally tuned, SGD generalizes better than Adam, particularly under noisy conditions. These results confirm the empirical results in the literature. Since its first appearance [32], Adam has often been preferred over SGD due to its ability to converge more quickly toward the minimum of a loss function, leading to a more efficient training process with lower training losses. This advantage is primarily attributable to Adam’s adaptive learning rate mechanism, which enables it to make informed parameter updates by considering both the first and second moments of the gradients. However, despite Adam’s superior performance during training, some authors have observed that models optimized with SGD generalize better to unseen test data. For example, SGD displayed better generalization ability than adaptive optimization methods, such as Adam, in [33], [34], [35], [36], [37], [38]. Despite these observations, Adam remains widely

used as an optimization tool in deep learning [39], [40], [41], [42], [43].

## VII. CONCLUSIONS

This paper proposes a double-Bayesian learning framework from which the optimal learning rate for neural network training with SGD is derived (approx. 0.016). An extensive grid search showed that the derived learning rate and rates close to it performed better across different classification, segmentation, and object detection tasks. SGD consistently outperformed Adam across these tasks, regardless of training set size, except for one experiment. Adam performed best with very small learning rates, which is consistent with the literature. Momentum did not significantly affect Adam, whereas higher momentum values (0.4-0.8+) led to better results with SGD. Furthermore, SGD consistently outperformed Adam under noisy conditions. The performance gap widened at higher noise levels, indicating a greater robustness to noise by SGD. Adam achieved lower validation loss than SGD in several cases but failed to deliver better test performance, indicating a tendency toward overfitting. While SGD achieved the best overall performance, Adam reached its minimum validation set loss more quickly, which may explain its high popularity.

The proposed double-Bayesian framework is a new approach to decision-making. The question of when a classifier or predictor is optimal can be answered in new ways by describing a decision process as a combination of two Bayesian processes. Knowledge is distributed across these two processes, and it is impossible to access their outcomes simultaneously. The imposed uncertainty and measurement limitations are reminiscent of similar phenomena in other areas, such as Heisenberg's Uncertainty Principle in physics. It is also worth mentioning that the golden ratio plays a prominent role in this information-theoretical approach. It defines an equilibrium in which the uncertainty of one of the two processes involved is minimized.

In summary, the double-Bayesian approach offers new insights into learning and neural network training. It gives new meaning to the momentum term in SGD and explains why its use is beneficial, which extends beyond the traditional understanding of it as a smoothing term. The derived learning rate will yield less biased models, thereby improving their explainability and interpretability.

## ACKNOWLEDGMENTS

This research was supported in part by the Lister Hill National Center for Biomedical Communications of the National Library of Medicine (NLM), National Institutes of Health (NIH). The contributions of the NIH author(s) are considered Works of the United States Government. The findings and conclusions presented in this paper are those of the author(s) and do not necessarily reflect the views of the NIH or the U.S. Department of Health and Human Services. The work has also been funded in part with federal funds from the National Institute of Allergy and Infectious Diseases (NIAID), National Institutes of Health, Department of Health and Human Services under

BCBB Support Services Contract HHSN316201300006W/75N93022F00001 to Guidehouse Digital. This work utilized the high-performance computational capabilities of the Biowulf Linux cluster at the National Institutes of Health, Bethesda, MD (<http://biowulf.nih.gov>).

## REFERENCES

- [1] J. Bergstra and Y. Bengio, "Random search for hyper-parameter optimization." *Journal of machine learning research*, vol. 13, no. 2, 2012.
- [2] H. Li, P. Chaudhari, H. Yang, M. Lam, A. Ravichandran, R. Bhotika, and S. Soatto, "Rethinking the hyperparameters for fine-tuning," *arXiv preprint arXiv:2002.11770*, 2020.
- [3] A. Krizhevsky, I. Sutskever, and G. Hinton, "Imagenet classification with deep convolutional neural networks," in *Advances in neural information processing systems*, 2012, pp. 1097–1105.
- [4] K. Simonyan and A. Zisserman, "Very deep convolutional networks for large-scale image recognition," *arXiv preprint arXiv:1409.1556*, 2014.
- [5] K. He, X. Zhang, S. Ren, and J. Sun, "Deep residual learning for image recognition," in *Proceedings of the IEEE Conference on computer vision and pattern recognition*, 2016, pp. 770–778.
- [6] R. Jacobs, "Increased rates of convergence through learning rate adaptation," *Neural networks*, vol. 1, no. 4, pp. 295–307, 1988.
- [7] D. Kingma and J. Ba, "Adam: A method for stochastic optimization," *arXiv preprint, arXiv:1412.6980*, 2014.
- [8] J. Duchi, E. Hazan, and Y. Singer, "Adaptive subgradient methods for online learning and stochastic optimization." *Journal of machine learning research*, vol. 12, no. 7, 2011.
- [9] T. Tieleman and G. Hinton, "Lecture 6.5-rmsprop: Divide the gradient by a running average of its recent magnitude," *COURSERA: Neural networks for machine learning*, vol. 4, no. 2, pp. 26–31, 2012.
- [10] Y. Bengio, "Practical recommendations for gradient-based training of deep architectures," in *Neural networks: Tricks of the trade*. Springer, 2012, pp. 437–478.
- [11] I. Sutskever, J. Martens, G. Dahl, and G. Hinton, "On the importance of initialization and momentum in deep learning," in *International Conference on Machine Learning*, 2013, pp. 1139–1147.
- [12] J. Spall, "Adaptive stochastic approximation by the simultaneous perturbation method," *IEEE transactions on automatic control*, vol. 45, no. 10, pp. 1839–1853, 2000.
- [13] S. Jaeger, "Double-Bayesian learning," arXiv:2410.12984v1 [cs.LG], October 2024. [Online]. Available: <https://arxiv.org/abs/2410.12984>
- [14] V. Bui, H. Yu, K. Kantipudi, Z. Yaniv, and S. Jaeger, "Evaluating the performance of hyperparameters for unbiased and fair machine learning," in *Medical Imaging 2024: Image Processing*, vol. 12926. SPIE, 2024, pp. 275–287.
- [15] C. Shannon, "A mathematical theory of communication," *Bell System Technical Journal*, vol. 27, no. 3, pp. 379–423, 1948.
- [16] T. Mitchell, *Machine learning*. McGraw-Hill, 1997.
- [17] S. Jaeger, "The golden ratio in machine learning," in *IEEE Applied Imagery Pattern Recognition Workshop (AIPR)*, 2021, pp. 1–7.
- [18] M. Livio, *The Golden Ratio*. Random House, Inc., 2002.
- [19] Y. LeCun, L. Bottou, G. Orr, and K. Müller, "Efficient backprop," in *Neural networks: Tricks of the trade*. Springer, 2012, pp. 9–48.
- [20] G. Huang, Z. Liu, and K. Q. Weinberger, "Densely connected convolutional networks," *CoRR*, vol. abs/1608.06993, 2016.
- [21] "Ultralytics YOLOv8," 2023, <https://github.com/ultralytics/ultralytics>, last accessed September 2023.
- [22] Y. LeCun, C. Cortes, and C. Burges, *The MNIST Database*, last accessed May 21, 2024. [Online]. Available: <http://yann.lecun.com/exdb/mnist/>
- [23] K. He, X. Zhang, S. Ren, and J. Sun, "Delving deep into rectifiers: Surpassing human-level performance on imagenet classification," in *Proceedings of the IEEE international conference on computer vision (ICCV)*, 2015, pp. 1026–1034.
- [24] Y. Liu, Y.-H. Wu, Y. Ban, H. Wang, and M.-M. Cheng, "Rethinking computer-aided tuberculosis diagnosis," in *Proceedings of the IEEE/CVF conference on computer vision and pattern recognition*, 2020, pp. 2646–2655.
- [25] "TBX11K chest X-ray dataset," 2020, <https://mmcheng.net/tb/>, last accessed July 2023.
- [26] S. Edwardsson and A. Rizzoli, "COVID-19 X-ray dataset," 2020, <https://github.com/v7labs/covid-19-xray-dataset>, last accessed September 2023.
- [27] T. Lin, M. Maire, S. Belongie, J. Hays, P. Perona, D. Ramanan, P. Dollár, and C. L. Zitnick., "Microsoft COCO: Common objects in context," in *Computer vision—ECCV: 13th European conference*, 2014, pp. 740–755.

- [28] M. P. K. Silamut, R. J. Maude, S. Jaeger, and G. Thoma, "Image analysis and machine learning for detecting malaria," *Translational research: the journal of laboratory and clinical medicine*, vol. 194, pp. 36–55, 2018.
- [29] "NLM malaria dataset," 2018, <https://lhncbc.nlm.nih.gov/LHC-research/LHC-projects/image-processing/malaria-datasheet.html>, last accessed July 2023.
- [30] M. Everingham, L. Van Gool, C. K. Williams, J. Winn, and A. Zisserman, "The Pascal Visual Object Classes (VOC) challenge," *International journal of computer vision*, vol. 88, pp. 303–338, 2010.
- [31] S. Chaudhury and T. Yamasaki, "Robustness of adaptive neural network optimization under training noise," *IEEE Access*, vol. 9, pp. 37 039–37 053, 2021.
- [32] D. P. Kingma and J. Ba, "Adam: A method for stochastic optimization," in *arXiv e-prints*, 2014.
- [33] M. Hardt, B. Recht, and Y. Singer, "Train faster, generalize better: Stability of stochastic gradient descent," in *International conference on machine learning*, 2016, pp. 1225–1234.
- [34] A. C. Wilson, R. Roelofs, M. Stern, N. Srebro, and B. Recht, "The marginal value of adaptive gradient methods in machine learning," *Advances in neural information processing systems*, vol. 30, 2017.
- [35] N. S. Keskar and R. Socher, "Improving generalization performance by switching from Adam to SGD," in *arXiv e-prints*, 2017.
- [36] J. Chen, D. Zhou, Y. Tang, Z. Yang, Y. Cao, and Q. Gu, "Closing the generalization gap of adaptive gradient methods in training deep neural networks," in *IJCAI*, 2020.
- [37] Y. Zhou, B. Karimi, J. Yu, Z. Xu, and P. Li, "Towards theoretically understanding why SGD generalizes better than Adam in deep learning," *Advances in Neural Information Processing Systems*, vol. 33, pp. 21 285–21 296, 2020.
- [38] Z. Xie, X. Wang, H. Zhang, I. Sato, and M. Sugiyama, "Adaptive inertia: Disentangling the effects of adaptive learning rate and momentum," in *International conference on machine learning*, 2022, pp. 24 430–24 459.
- [39] G. Balakrishnan, A. Zhao, M. R. Sabuncu, J. Guttag, and A. V. Dalca, "Voxelmorph: a learning framework for deformable medical image registration," *IEEE transactions on medical imaging*, vol. 38, pp. 1788–1800, 2019.
- [40] L. Chen, P. Bentley, K. Mori, K. Misawa, M. Fujiwara, and D. Rueckert, "Self-supervised learning for medical image analysis using image context restoration," *Medical image analysis*, vol. 58, p. 101539, 2019.
- [41] X. Li, L. Yu, H. Chen, C.-W. Fu, L. Xing, and P.-A. Heng, "Transformation-consistent self-ensembling model for semisupervised medical image segmentation," *IEEE Transactions on Neural Networks and Learning Systems*, vol. 32, pp. 523–534, 2020.
- [42] I. D. Apostolopoulos and T. A. Mpesiana, "Covid-19: automatic detection from X-ray images utilizing transfer learning with convolutional neural networks," *Physical and engineering sciences in medicine*, vol. 43, pp. 635–640, 2020.
- [43] K. Armanious, C. Jiang, M. Fischer, T. Küstner, T. Hepp, K. Nikolaou, S. Gatidis, and B. Yang, "MedGAN: Medical image translation using gans," *Computerized medical imaging and graphics*, vol. 79, p. 101684, 2020.